75th International Astronautical Congress (IAC), Milan, Italy, 14-18 October 2024.

IAC-24-A6

A numerical model for CFRP fragmentation under hypervelocity impacts

S. Lopresti[a]*, A. Abiti[b], L. Olivieri[a,c], C. Giacomuzzo[a], E.M. Polli[d], A. Francesconi[a,c]

[a]*CISAS "G. Colombo", University of Padova, Via Venezia 15, 35131 Padova, Pd, Italy*
[b]*University of Padova, Via VIII Febbraio 2, 35122 Padova, Pd, Italy*
[c]*DII, University of Padova, Via Venezia 15, 35131 Padova, Pd, Italy*
[d] *DAER, Politecnico di Milano, Via La Masa, 34, 20156 Milano, Mi, - Italy*
* Corresponding Author

Abstract

Space debris represents a substantial hazard to satellites, posing the risk of collisions that can lead to partial or total break-ups. In the last years, carbon fiber reinforced plastic (CFRP) has started to be used increasingly more extensively on spacecraft due to its high strength-to-weight ratio. Despite its wide use, to date its fragmentation behaviour under hypervelocity impact conditions has not yet been fully understood and modelled. In this context, this paper presents a numerical model for CFRP fragmentation recently developed by the Space Debris Group of the University of Padova. The model is constructed and validated from experimental data, collected both from dedicated tests and literature; it consists in a set of semi-empirical equations describing the fragmentation pattern on CFRP plates and the distribution of generated fragments. The model input includes various parameters, such as the impact velocity, the impact angle, and the CFRP layup, to determine the fragmentation behaviour. It is also capable to determine delamination effects and the extension of the damaged area in function of the material fiber orientations and weaves. Finally, the developed model is currently under inclusion into the material library of the Collision Simulation Tool Solver (CSTS), a software developed by the research group to describe hypervelocity break-up and fragmentation processes.
Keywords: Space debris, CFRP, Hyper-velocity impact.

Acronyms and abbreviations

CFRP	Carbon Fiber Reinforced Plastic
CSTS	Collision Simulation Tool Solver
GEO	Geostationary Earth Orbit
HVI	Hypervelocity Impact
IADC	Inter-Agency Space Debris Coordination Committee
LEO	Low Earth Orbit
A	Major delamination length
a	Fragment larger size
B	Minor delamination length
D	Diameter
K	Kinetic energy
N_{PLY}	Number of plies
R	Radius
R^2	Coefficient of determination
t	Thickness
v	Velocity
θ	Impact angle

1. Introduction

Improving the understanding of the space environment, debris and being able to predict its evolution is of fundamental importance in order to be able to protect critical infrastructure in space and ensure the long-term sustainability of the space environment [1]. Space debris has been a problem for the space exploration that has been aware of since the early 1960s, but it is only from the following decades that international awareness has been created [2] [3]. A significant milestone was reached in 2002 with the publication of the "IADC Space Debris Mitigation Guidelines" by the Inter-Agency Space Debris Coordination Committee (IADC), a global governmental forum dedicated to coordinating space debris activities. This document, which is regularly updated, serves as the foundation for non-binding international policies, national legislations, and technical standards aimed at mitigating space debris. The IADC guidelines primarily focus on safeguarding the sustainability and safety of key orbital regions, specifically Low Earth Orbits (LEOs) and Geostationary Earth Orbits (GEOs). To address the space debris problem, several countermeasures can be employed, broadly categorized as either active or passive. Active countermeasures involve techniques such as debris removal and collision avoidance maneuvers, while passive measures typically involve physical shielding. Various types of shields, constructed from different materials and designs, serve to protect satellites and their systems from the effects of hypervelocity impacts [4]. The use of shields finds greatest effectiveness in preventing damage from millimetre and sub-millimetre-sized debris. To prevent damage from larger debris, these are often not sufficient and avoidance manoeuvres should be used, if possible. The study of hypervelocity impact phenomena is therefore critical in developing more effective passive protections for spacecraft. Understanding the physical mechanisms of these impacts can lead to the design of shields with enhanced performance, capable of withstanding the extreme conditions created by space debris collisions.

In the reminder of this paper, the development and implementation of a CFRP fragmentation model is presented. Section 2 introduces the mechanisms involved in collisions with isotropic materials and section 3 describes the complexity of the response of a non-isotropic composite. Section 4 presents the dataset used and how it was processed.

Section 5 presents the new CFRP model, the interpolation of the data, and the main limitations of the model.
Finally, section 6 shows how the new model is being integrated within the CSTS code

2. Impact physics for isotropic materials

In order to understand hypervelocity impacts, it is first essential to understand the order of magnitude of velocities, so as to quantify the energies of the objects involved.
The orbital velocity v_{orb} of an object in a circular orbit around a larger mass can be derived from:

$$v_{orb} = \sqrt{\gamma * \frac{m_T}{r}} \qquad (1)$$

The gravitational parameters for the Earth can be defined as follows:

$$\gamma * m_T = 6.67 * 10^{-11} * 5.98 * 10^{24} = 3.99 * 10^{14} \frac{m^3}{s^2} \qquad (2)$$

As a result, in-space collisions among objects on same altitudes but different orbital planes can reach relative velocities up to 6 km/s for GEOs and 15 km/s for LEOs; in case of micrometeoroids from deep space intersecting Earth's orbit, collision velocities can increase up to one order of magnitude [5].
Hypervelocity impacts (HVI) are defined as collisions in which the speed of the projectile is greater than the speed of sound propagation in the target material, that is the speed at which pressure waves propagate. The impact phenomenon on a plate of isotropic material such as aluminium, can be divided into two phases: The interaction between the projectile and the target and the diffusion of the generated debris cloud.
In the first phase, two compressive elastic-plastic waves are generated and propagate moving away from the interface respectively inside the projectile and the plate. At the same time, rarefaction waves generated due to the finite diameter of the projectile are transmitted transmitted in the direction of the axis of symmetry. The latter waves cause material to be ejected, both by the plate and the projectile, in the direction opposite to that of impact. Subsequently, the compressive elastic-plastic wave reaches and is reflected from the back of the slab, generating a tensile stress situation in the backside, which, if the material failure limit is exceeded, generates an effect called spall. The spall is the separation of the back layer of the affected slab that is generated even in the case where complete perforation of the slab is not achieved. In general, the whole process of fracture can be interpreted as a phenomenon of multiple spalls starting from the free surface.

Fig. 1: Result of an HVI impact with spall formation (credits: ESA).

One of the phenomena encountered, in the context of a hypervelocity impact, is the phase transition affecting both the projectile and the plate. Indeed, the high energy of the collision process generates, at propagation, a sharp increase in temperature [6]. For an aluminium-on-aluminium impact, the material starts to liquefy for impact velocities of about 5 km/s and begins to vaporize at 10 km/s. For on-orbit impacts between space debris and shielding structures, this phenomenon is dominant within the debris clouds and inevitably affects shield performance.
An hypervelocity impact eventually creates debris clouds whose characteristics depend on a number of factors, including the material and shape of the projectile and slab itself, the angle of collision and the speed at which it occurs, the ambient temperature and others.

3. Hypervelocity impacts on CFRP

The damage mechanism of a fiber-reinforced composite, when subjected to hypervelocity impact, is in some respects different from that obtained for classical materials and can be divided into the following stages: crater formation, fiber rupture, fiber fraying and detachment, matrix cracking, creation of new surfaces, and finally delamination of the layers. As the velocity of the projectile increases, the kinetic energy of the projectile also increases and consequently so do the deformation rates of the materials composing the target. The physics of HVI on composite materials is particularly complex because the pressure waves, generated by the impact, do not move within a homogeneous material but are subjected to multiple phases where each ply acts as a surface that partly reflects and partly transmits the stress waves. This creates, for each ply, a situation similar to that exposed in the previous paragraph for a single sheet of isotropic material. The waves, initially compressive, are reflected and create a state of tensile stress that first causes the composite to reach failure stress and finally generates delamination not only of the external but also of the intermediate plies.

A sequence of images describing the evolution of the debris cloud of an HVI on a CFRP plate can be seen in Fig. 2. Similar to other materials already discussed, the cloud can be divided in two and studied in two different areas: one originates from the front of the plate (front cloud), especially from the impact perimeter between projectile and target, and propagates in the direction opposite to the velocity vector of the projectile; the other (rear cloud) propagates instead in the direction concordant to this and is larger in size. The latter is the most dangerous as it propagates internally to the spacecraft and can create appreciable damage to the spacecraft structure and its instrumentation. In frame 1 of Fig. 2, the aluminium sphere used as a projectile (right), the bright flash generated by the plasma, and the first stage of formation of the rear cloud can be clearly seen. The back cloud is also highlighted in frame 2 - (e). In the third image are represented, in order:

- The increased thickness of the plate around the impact crater (b). This effect is due to delamination of the inner layers.
- The structure of the frontal cloud showing two areas: An inner structure (c) and an outer bubble (d). This differentiation becomes evident only at high impact velocities and late moments of impact. The two zones have different densities and also different velocities. In fact, the inner structure contains fragments from both the plate and the projectile and has higher density and lower velocity. The outer bubble, on the other hand, is composed of more dispersed debris from the surface lamina of the target.

Finally, in the last frame, the detachment of the frontal and back surface lamina (a) can be clearly seen.

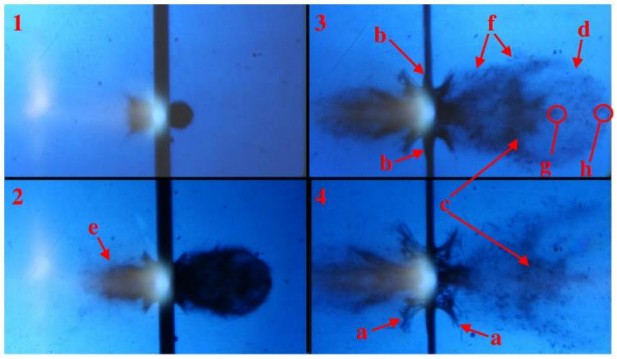

Fig.2: Shadowgraph sequence of an HVI on a CFRP plate; the time step between consecutive frames is of 14μs [7]

The damage that is created around the impact zone depends heavily on the type of carbon fiber used on the fiber configuration. An example for a unidirectional ply plate is shown in Fig. 3. The crater created is not homogeneous but very irregular due to the disordered fragmentation of the fibers. On the front face of the slab, a long delamination zone can be observed, the width is slightly greater than the front diameter of the crater. In the case of unidirectional ply, the delamination extends along the preferential direction of the fibers. The delamination region is more homogeneous around the crater when it is woven carbon. The same delamination can also be seen on the back face of the plate.

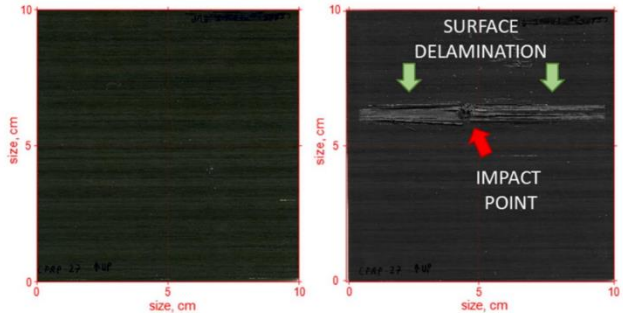

Fig. 3 Damage generated from an HVI on a UD CFRP. Front face before (left) and after (right) impact. [8]

4. Collision data from laboratory experiments

The data analysed in the study were collected over the years by the CISAS research center, in collaboration with other international research entities, using the hypervelocity impact facility of the University of Padova [9] [10] [11]. In total, data regarding 176 tests obtained from literature and the internal test database [12] [13]were analysed, broken down as follows:

Table. 1 Overview of the date used for the study.

Type	Number of plys	Number of tests
CFRP plates, epoxy-UD, HS carbon fiber with medium modulus	12	4
	16	34
	24	26
	32	34
	40	9
Sandwich CFRP-Honeycomb with UD carbon fiber	Not recorded	55
Sandwich CFRP-Honeycomb with carbon fiber tissue	16	14

The projectiles used for testing are aluminium spheres with diameters of 0.8 mm, 1 mm, 1.5 mm, 1.9 mm, 2.3 mm and 2.9 mm. Smaller diameters were also used for HC-CFRP UD sandwiches: 0.1 mm, 0.3 mm and 0.59 mm. The projectiles were accelerated to velocities ranging from 2 km/s to 5.5 km/s. Most impacts occurred at an angle of 0° but tests at angles of 15°, 30° and 45° were also considered.

For all experiments, once the damage on the targets was detected, the hole diameter and the length of the two main directions of delamination were measured. This was done for both the front and back faces. These measurements were acquired by taking a high-resolution image of the front and back surface of the target after each test using a scanner. From this scan, the diameter of the crater was measured with an image analysis code implemented in Matlab™.

Defining what the actual crater area is for such a jagged surface is a challenging topic. For these experiments it was decided to follow this procedure. First, the user manually selects the area of damage in a coarse manner. This area is defined as the region that includes all visible fiber fracture points. Next, the software detects the perimeter lines of the damaged area, using the standard Hough transform extraction technique. The intersection of the detected lines determines the damage area, from which the equivalent diameter D_c is then derived. The uncertainty on D_c is mainly related to the arbitrary selection made at the

beginning by the user. Although this process extends the measurement time, it allows the uncertainties to be reduced compared to a manual measurement by calliper.

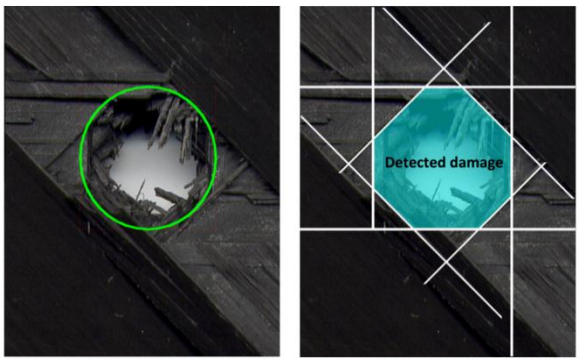

Fig. 4: Hole generated from the projectile. Example of the coarse area human selected (left) and of the area software selected. [7]

For a selection of the experiments [8], the projectile and target were also weighed before the tests so that their weight was compared with the plate and the collected fragments, measured after the experiment. For these cases, the fragments were classified and thanks to an automatic image analysis code their size distribution was obtained.

In order to have more data, test results on CFRP plates with slightly different layup, fiber and resin characteristics were analysed together. This partially increased the scattering of the experimental data but at the same time made it possible to generate empirical models representative not of a specific type of composite material but of the entire family.

5. CFRP fragmentation model

The CFRP model developed in this work is based on the following assumptions. The basic idea behind this model is to use three separate damage regions, the first close to the impact point and the other two extended far from the impact location to represent surface delamination, on the front and rear face (see fig. 5). In terms of fragments size, the former produces small fragments with comparable perpendicular dimensions, whereas long needle-shaped fragments detach from the latters. These last are characterised by one dimension being much larger than the others. For each of these regions, the main geometrical parameters are defined as function of the collision data.

Graphs relating the main geometric quantities of damage to the kinetic energy (K) of the projectile are presented in the next paragraph. In the following discussion, “D” will indicate the diameter of the crater, “A” will indicate the major delamination length and “B” will indicate the minor delamination length (Fig. 5). A and B refer only to the surface delamination, which, depending on the impact velocity, affects only the first ply or two.

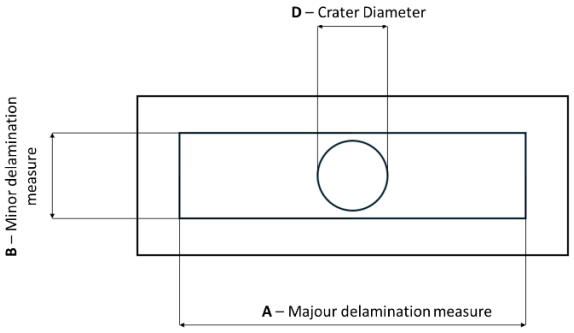

Fig. 5: Image parameters of the plates

5.1. Data analysis

Analysing the experimental data on the CFRP plates, it can be noted that the average diameter extension of crater D and that of B are comparable, with the latter being larger in size. The frontal parameters are also similar to the posterior ones. A comparison of these magnitudes for the 16-ply plates is shown in Fig. 6.

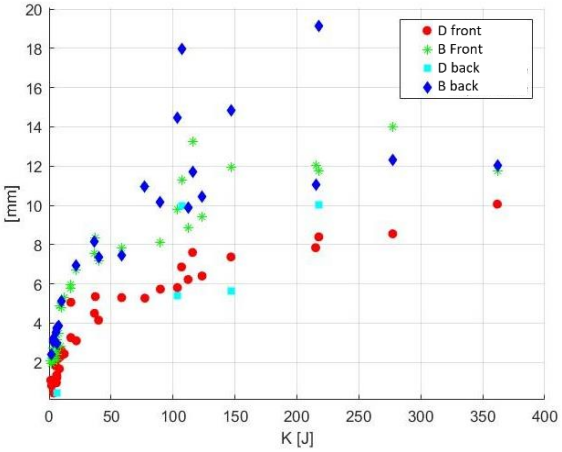

Fig. 6: Diameter of the hole and delamination length, related over impact energy (16 Ply)

Regarding the major direction of delamination in the case of unidirectional ply, this extends for a length about an order of magnitude longer than the minor one, in the direction in accordance with the fibre. Also in this case, the front and rear lengths are comparable.

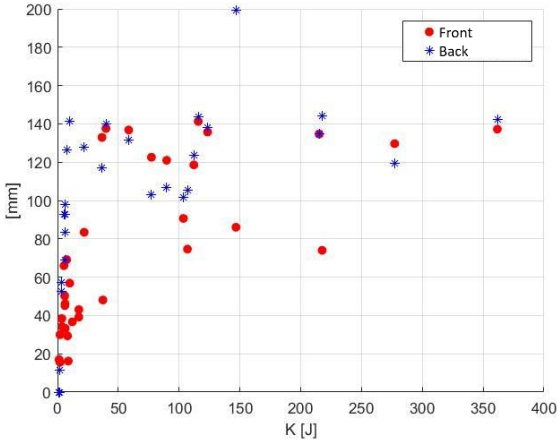

Fig. 7: Minor delamination length (front and back) as a function of projectile kinetic energy K for 16 ply CFRP sheets

Two other parameters, measured as part of the experimental tests, and which were analysed, are A_{MAX} and B_{MAX}: A_{MAX} is the maximum size of the longest fragment, B_{MAX} on the other hand is its smallest size, measured accordingly. It can be seen in Fig. 8 that there is a strong proportionality between A_{MAX} and the value of the largest delamination length A (A_{MAX} is approximately half of A). The measured values of B_{MAX}, on the other hand, are much more disordered: this is probably due to the small values they take on. The trend shown by A_{MAX} is expected to change as the size of the plates increases. Indeed, it is likely that fragments as large as half the length of the largest delamination are increasingly unstable as their length increases and thus undergo further fragmentation due to the reflection of mechanical stress waves. This hypothesis will be evaluated in the future through a dedicated experimental campaign on larger plates.

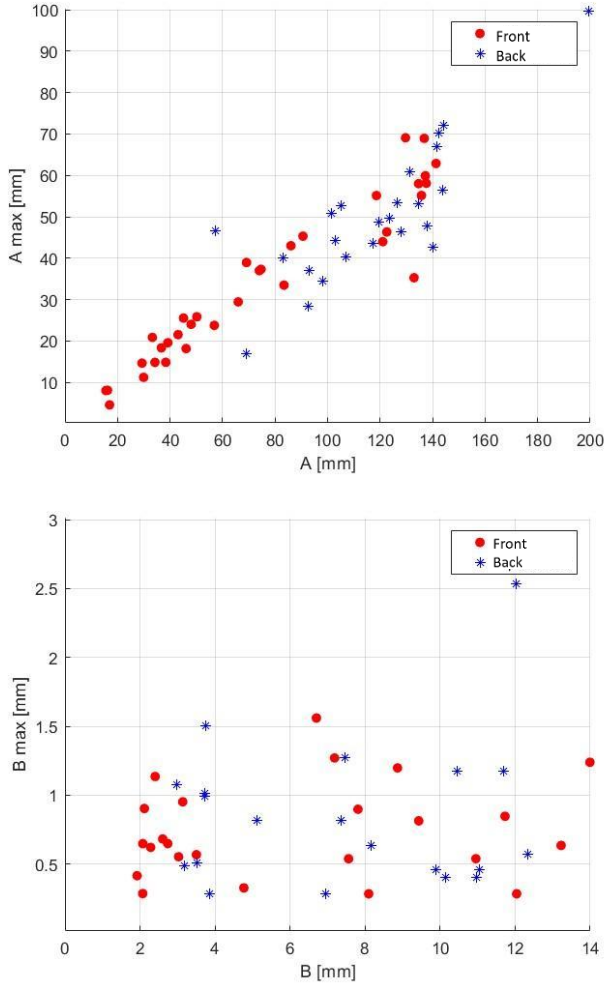

Fig. 8: Graphs comparing the length of AMAX versus A (top) and that of BMAX versus B (bottom) for 16-ply CFRP plates.

Finally, Fig. 9 shows the comparison of crater frontal diameter growth on the basis of kinetic energy K for all the slabs analysed, broken down by ply number. The comparison does not take into account the thickness of the plates; in fact, the 12-ply plates show a much higher performance than the 40-ply plates precisely because they have a larger thickness. In general, an almost logarithmic growth trend can be seen.

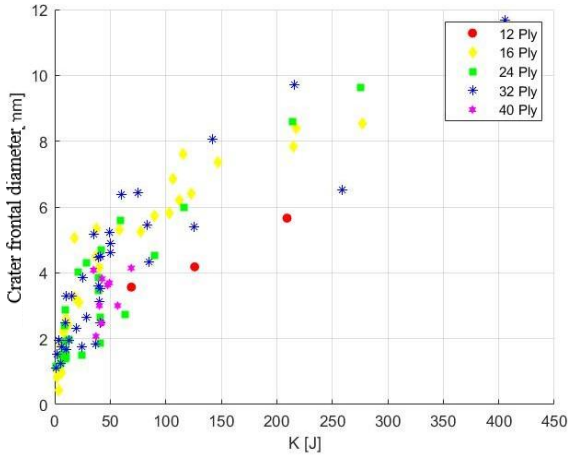

Fig. 9: Comparison of frontal crater diameter as a function of projectile kinetic energy K for CFRP plates

5.2. Main parameters equations

The study focused on CFRP plate data with the idea of creating models that could relate the main damage parameters, described above, to the characteristics of the projectile, target and impact kinematics.

Ply number and thickness are the only information entered for the target material, in order to take into account the lamination performed for the plate. Otherwise, the models will be descriptive only of CFRP with unidirectional ply, laminated in such a way as to seek orthotropicity of the plate.

To generate the relationships, given the high number of independent variables to be considered, a non-linear interpolation on a function of the type was chosen:

$$Y = \alpha * D_P^{\beta} * V_P^{\gamma} * (\cos\theta)^{\delta} * N_{PLY}^{\varepsilon} * t^{\omega} \quad (4)$$

Where "D_p" is the projectile diameter, "V_p" is the projectile velocity, "θ" is the impact angle, and "t" is the thickness of the plate

The data presented in the graph have already been processed and have a 95% confidence level.

below are some considerations of the models presented on the next page

- D_{Front}: The regression coefficient is reasonably accurate, with the largest source of uncertainty coming from the cosine of the impact angle, as expected
- A_{Front}: The data for the longer frontal delamination length have more scattering due to differences in materials and measurement inaccuracies. This slightly lowers the regression coefficient.
- B_{Front}: As for the crater frontal diameter, the cosine of the impact angle is the major source of uncertainty.
- D_{Back}: In this case there was limited data available, as the back diameter was only recordable in those samples that had reached

full penetration. Because of this, a model with five independent variables would have been too unstable, and it was decided to eliminate the influence of angle and ply number. The model will have to be updated when more data will be available.

- A_{Back}: This model presents higher uncertainties than A_{Front}'s model. In general, due to the complexity of impact physics, models concerning the back face of the plates are more inaccurate.
- B_{Back}: The value of dimension B is generally more repeatable than that of dimension A. Once again, compared with the longer delamination length, this model for the back face has lower uncertainties and better correlation.
- A_{Max}: In this case, the maximum fragment size was related to the maximum delamination length, revealing a good correlation between these two parameters.
- B_{Max}: In this case, the large noise in the data did not allow for correlations with high R2 values so the two models are unreliable. More data would be needed to improve the correlation coefficient. The best models were found by relating B_{Max} to A_{Max}.

Frontal diameter of the crater, D_{Front}

$$D_{Front} = 0.0015 * D_P^{1.3679} * V_P^{0.8202} * (\cos\alpha)^{0.4715} * N_{PLY}^{0.2977} * t^{-0.3937} \quad (5)$$

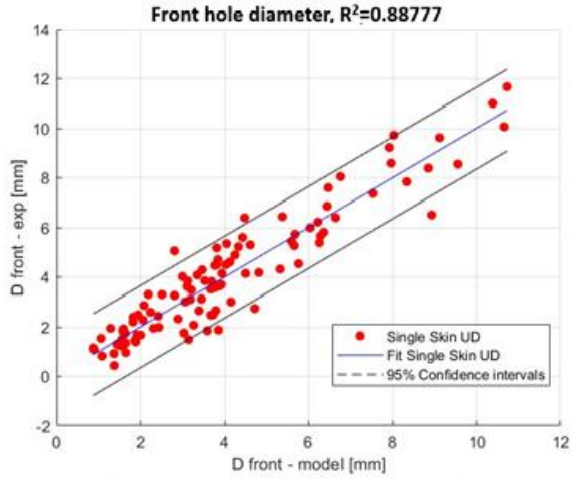

Fig. 10: Non-linear regression for crater frontal diameter

Rear crater diameter, D_{Back}

$$D_{Back} = 0.00057 * D_P^{2.0725} * V_P^{0.9604} * t^{-0.2136} \quad (6)$$

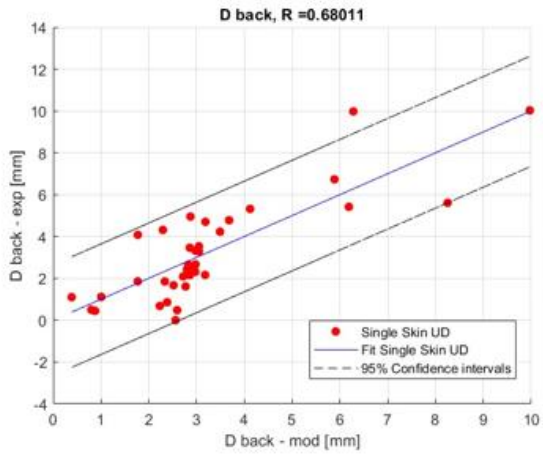

Fig. 11: Non-linear regression for the back diameter of the crater

Major frontal delamination length, A_{Front}

$$A_{Front} = 1.0353 * D_P^{0.7889} * V_P^{0.346} * (\cos\alpha)^{0.5757} * N_{PLY}^{0.2436} * t^{-0.4185} \quad (7)$$

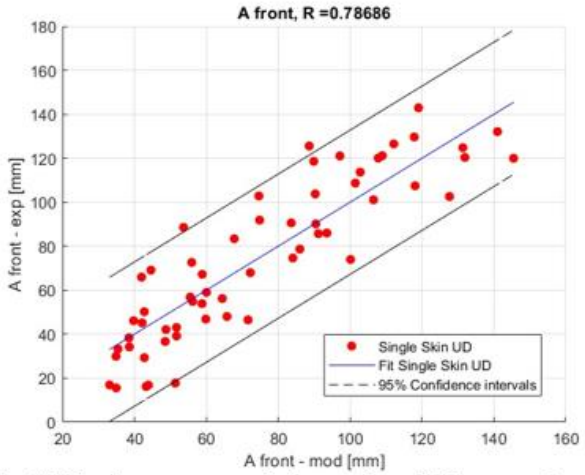

Fig. 12: Non-linear regression for longest frontal delamination length

Major rear delamination length, A_{Back}

$$A_{Back} = 133.0608 * D_P^{0.6254} * V_P^{0.8638} * (\cos\alpha)^{-0.1641} * N_{PLY}^{-3.5153} * t^{2.5739} \quad (8)$$

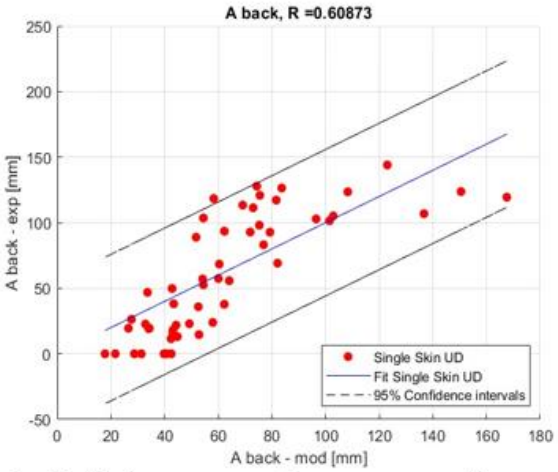

Fig. 13: Non-linear regression for major posterior delamination length

Minor frontal delamination length, B_{Front}

$$B_{Front} = 0.0042 * D_P^{1.2381} * V_P^{0.6951} * (\cos\alpha)^{0.455} * N_{PLY}^{0.4348} * t^{-0.1221} \quad (9)$$

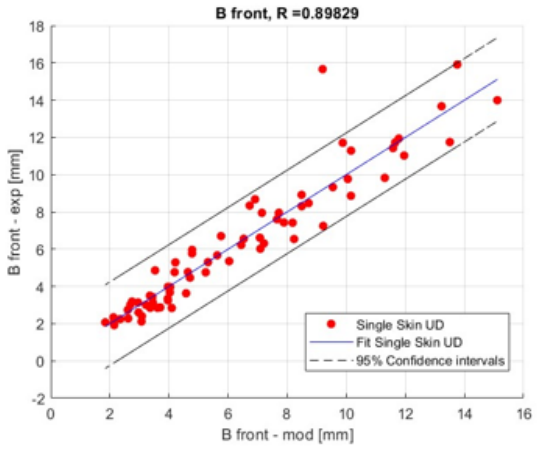

Fig. 14: Non-linear regression for minor frontal delamination length

Minor rear delamination length, B_{Back}

$$B_{Back} = 0.00115 * D_P^{1.0383} * V_P^{0.5351} * (\cos\alpha)^{0.2843} * N_{PLY}^{1.9463} * t^{-1.8084} \quad (10)$$

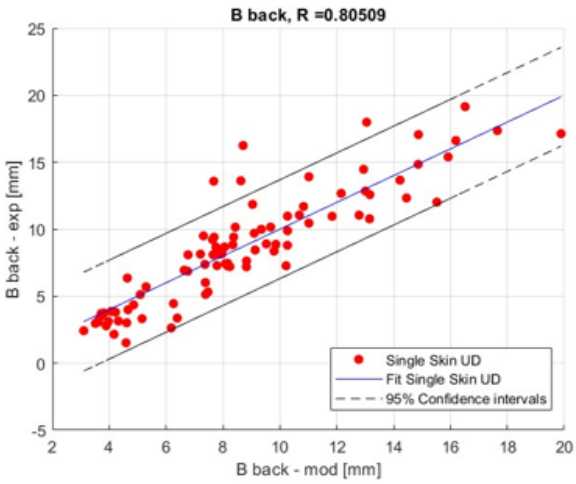

Fig. 15: Non-linear regression for minor posterior delamination length

Size of the delamination fragments length $A_{Max,front}$ and $A_{Max,back}$:

$$A_{Max\ front} = 0.4137 * A_{Front}^{1.029} \quad (11)$$

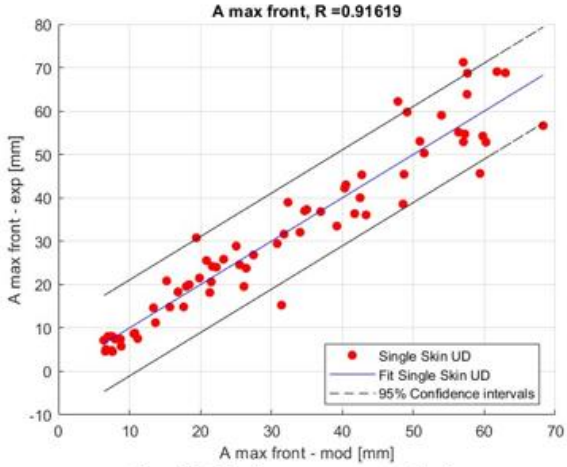

$$A_{Max\ back} = 0.4156 * A_{Back}^{0.9985} \quad (12)$$

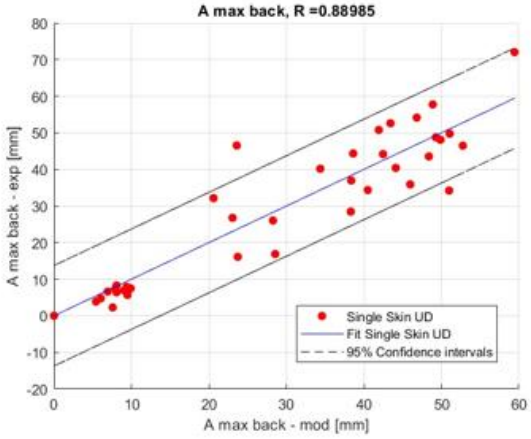

Fig. 16: Non-linear regression for the maximum size of the longest frontal (left) and posterior (right) fragment

Size of the delamination fragments length B_{Max} front e B_{Max} back

$$B_{Max\ front} = 0.1359 * A_{Max\ front}^{0.5270} \quad (13)$$

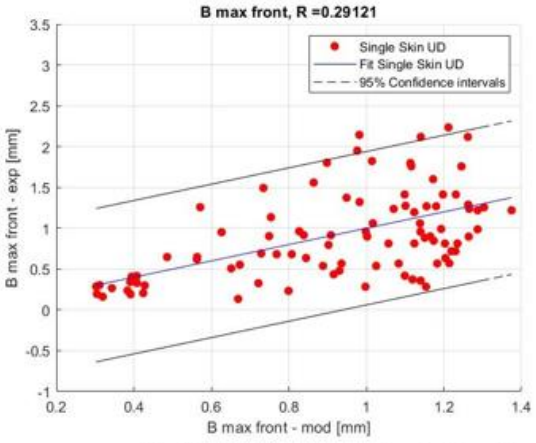

$$B_{Max\ back} = 0.1182 * A_{Max\ back}^{0.5296} \quad (14)$$

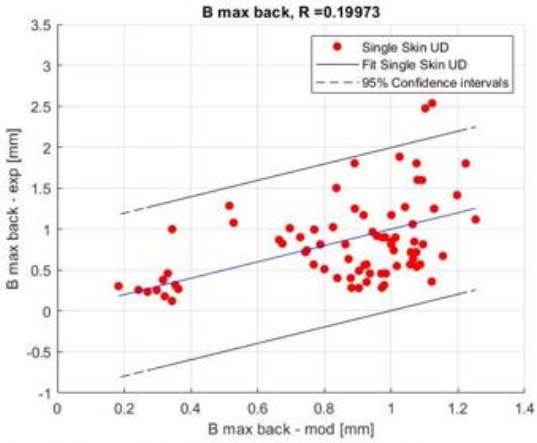

Fig. 17: Non-linear regression for the minimum size of the longest fragment front (top) and back (bottom)

7. Implementation in CSTS

With the aim of validating the models developed in Chapter 6, some of these were implemented as empirical models within the CSTS software, to check whether they improved the description of the debris cloud for CFRP materials provided by the code [14]. The code fragmentation model provides the description of the damage on the CFRP target as the sum of three contributions: a front face delamination, a central crater, and a back face delamination, as visible in Fig. 18. The delamination fragments are generated by sub-dividing the delamination area in needle-like objects whose maximum direction extends along fibre direction. In the current model, the delamination is controlled by six functions: three assess the perpendicular dimensions of the initial volume of material involved, and the other three regulate their subdivision into fragments.

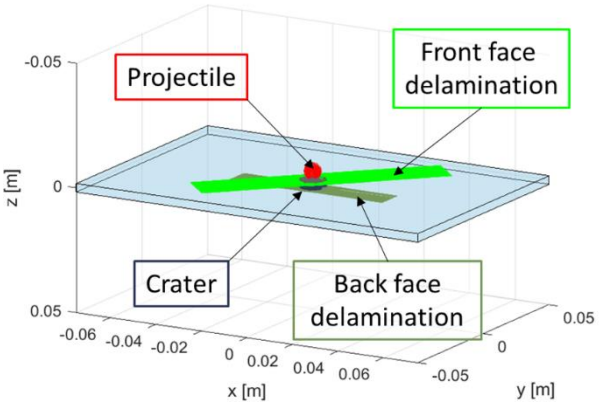

Fig. 18: Graphical visualization of the application of the fragmentation models in the CSTS code

For this work, the functions describing the delamination were modified: providing as input the frontal radius of the crater R_{CRAT}=D_{CRAT}/2, the velocity v and the diameter D_p of the projectile, the thickness t of the slab, its ply number N_{PLY} and the impact angle θ, it returns the following parameters as output:

- The three frontal delamination parameters along the x, y and z delamination directions: Specifically, x corresponds to the direction of maximum delamination, y to the direction of minimum delamination and z is the depth. For delamination along x and along y, (5) and (6) were used, respectively. For the depth of delamination, the original function was retained, where this is considered to be a single ply or two depending on conditions imposed on the relationship between projectile velocity and plate thickness. This parameter is difficult to measure and was deduced by observing x-ray images of impacts.
- The three back delamination parameters along the x, y and z delamination directions: In this case, (9) and (10) were used for delamination along x and along y. For delamination along z-axis, the same consideration done for front face are done.
- The number of fragments generated by the delamination alone (for the front and back faces): The delamination face is subdivided using a three-dimensional grid according to three parameters relating to the number of fragments along x, y and z. The shape and number of these are then derived from this grid.

The function, thus modified, was tested on the data of an experimental test not used for the creation of the models. Specifically, the results for the test were taken from data measured by Nishida [12]. In this paper, the debris distribution resulting from three hypervelocity impacts on CFRP sheets is analysed.

Fig.19 shows the results of the executed simulation. The graph presents in abscissa the maximum size of the debris, in this case named a, and in ordinate the cumulative number of fragments larger than a. The same graph shows the cumulative number of fragments for both the front side of the slab and the total. For the front side, three distributions are compared: The real one obtained from the Nishida tests (red), the one obtained from CSTS with the previously implemented method (black, the implemented model only covered the frontal cloud) and the one obtained thanks to the updated model (green). For the overall debris cloud, two distributions are compared: The real one derived from the data collected by Nishida (magenta) and the one obtained from the updated model (blue).

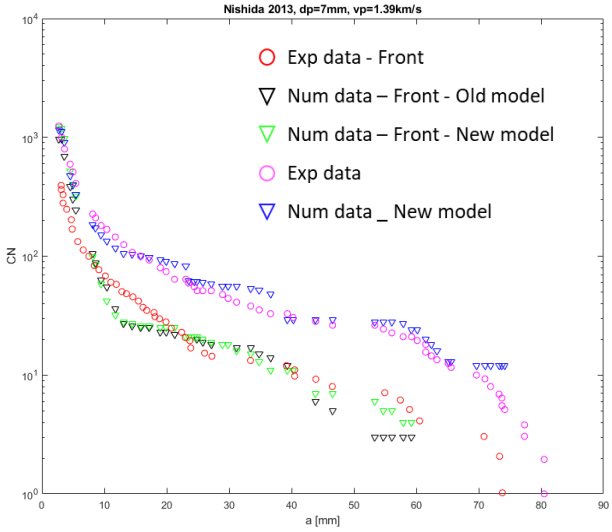

Fig. 19: Simulation results with Nishida parameters

It can be observed that the updated frontal distribution model slightly improves on the previous one. In particular, it shows a better fit to the original data in the range 30 mm – 60 mm. In general, due to the statistical nature of CSTS models that can reliably represent large populations of fragments, the punctual distribution of the largest debris (i.e. for less than 10 fragments, a > 60 mm) is still limited. However, as far as the overall distribution is concerned, this shows a very good adherence to the real data.

Since, for each point on the graph, the value of the cumulative number of debris for the Nishida data and the values output by CST are known, it was possible to calculate the correlation coefficient between the two series. The obtained value is R^2 = 0.9765, indicating an high correlation between model and experimental data.

8. Conclusions

In this paper the development of empirical models for the fragmentation of CFRP plates was presented. Analytical equations were obtained for all the parameters necessary to estimate the damage on the plates, including the delamination areas bot on the front and back faces.

The implementation of these equations within CSTS showed good results, quantified by a high correlation coefficient with the real data. This indicates a clear improvement with respect to the previously implemented model and allowed the full description of the debris cloud generated by the back plate, which was previously absent.

To improve the reliability of the collected results and expand their range of validity, further activities will be performed in the next months. First, it will be necessary to carry out further simulations on other test cases in order to confirm the models goodness on simple plate cases; after that, the same models should be tested and tuned against more complex geometries. In parallel, the empirical models are descriptive of impact situations within the described ranges. For much larger plates, for example, different behaviour is expected for parameters such as larger delamination size. The developed equations can easily be supplemented with data from experimental tests that will be carried out in the future, so as to achieve greater stability of correlation parameters and a reduction in uncertainties.

Acknowledgements

This work has been supported by the Italian Space Agency in the framework of the agreement n.2023-37-HH.0 “Attività tecnico-scientifiche di supporto a C-SSA/ISOC”.

Bibliography

[1] L. Anselmo, A. Rossi e C. Pardini, «Updated results on the long-term evolution of the space debris environment,» *Adv. Space Res.*, vol. 23, pp. 201-211, 1999.

[2] D. Kessler, N. Johnson, J. Liou e M. Matney, «The Kessler syndrome: Implications to future space operations,» *Adv. Astronaut.*, vol. 137, p. 210.

[3] D. Kessler e B. G. Cour-Palais, «Collision frequency of artificial satellites: The creation of a debris belt,» *Space Phys,* vol. 83, pp. 2637-2646, 1978.

[4] Y. Chen, Q. Tang, Q. He, L. Chen e X. Chen, «Review in hypervelocity impact of advanced space debris protection shields,» *Thin-Walled Structures,* vol. 200, 2024.

[5] P. Farinella e D. R. Davis, «Collision rates and impact velocities in the main asteroid belt,» *Icarus,* vol. 27, pp. 111-123, 1992.

[6] K. Wen, X. W. Chem e Y. Lu, «Research devekipment of hyperveloity impact protection using whipple shield: An overview,» *Defence Technology,* vol. 17, pp. 1864-1886, 2021.

[7] A. Francesconi, C. Giacomuzzo, S. Kibe, Y. Nagao e M. Higashide, «Effects of high-speed impacts on CFRP plates for space applications,» *Adv. Space Res,* vol. 50, pp. 539-548, 2012.

[8] L. Olivieri, C. Giacomuzzo e A. Francesconi, «Analysis of fragment distributions from carbon-fiber-reinforced composite panels subjected to hypervelocity impacts,» *AIAA Journal,* 2023.

[9] F. Angrilli, D. Pavarin, M. De Cecco e A. Francesconi, «Impact facility based upon high frequency two-stage light-gas gun.,» *Acta Astronautica,* vol. 53, pp. 185-189, 2003.

[10] A. Francesconi, D. Pavarin, A. Bettella e F. Angrilli, «A special design condition to increase the performance of two-stage light-gas guns.,» *Int. J. of Impact Engineering,* vol. 35, pp. 1510-1515, 2008.

[11] D. Pavarin e A. Francesconi, «Improvement of the CISAS high-shot-frequency light-gas gun.,» *Int. J. Impact Eng.,* vol. 29, pp. 549-562, 2003.

[12] M. Nishida, H. Kato, K. Hayashi e M. Higashide, «Ejecta size distribution resulting from hypervelocity impact of spherical projectiles on CFRP laminates,» *Procedia Engineering,* vol. 58, pp. 533-542, 2013.

[13] A. Francesconi, C. Giacomuzzo, S. Kibe, Y. Nagao e M. Higashilde, «Effects of high-speed impacts on CFRP plates for space applications,» *Advances in Space Research,* vol. 50, pp. 539-548, 2012.

[14] A. Francesconi, C. Giacomuzzo, L. Olivieri, G. Sarego, M. Duzzi, F. Feltrin, A. Valmorbida, D. Bunte, E. F. Deshmukh, J. Pervez, M. Zaake, T. Cardone e D. Wilde, «CST: A new semi-empirical tool for simulating spacecraft collisions in orbit,» *Acta Astronautica,* vol. 160, pp. 196-205, 2019.